Magnetism and site occupancy in epitaxial Y-rich yttrium iron garnet films

Tingyu Su, Shuai Ning, Eunsoo Cho, and Caroline A. Ross

Phys. Rev. Materials **5**, 094403 — Published 8 September 2021

DOI: 10.1103/PhysRevMaterials.5.094403

Magnetism and site occupancy in epitaxial Y-rich yttrium iron garnet films

Tingyu Su,[1] Shuai Ning,[2,3*] Eunsoo Cho,[2] Caroline A. Ross [2,‡]
[1]*Department of Mechanical Engineering, Massachusetts Institute of Technology, Cambridge, 02139, Massachusetts, USA*
[2]*Department of Materials Science and Engineering, Massachusetts Institute of Technology, Cambridge, 02139, Massachusetts, USA*
School of Materials Science and Engineering, National Institute for Advanced Materials, Nankai University, Tianjin, 300350, P. R. China.
[*]sning@nankai.edu.cn, [‡]caross@mit.edu

Abstract
Y-rich YIG (Y-YIG) thin films were grown on gadolinium gallium garnet substrates using pulsed laser deposition from a $YFeO_3$ target. The films are epitaxial on the substrate, and the unit cell of (001) and (111)-oriented Y-YIG undergoes a tetragonal or rhombohedral distortion respectively. The Y-YIG has lower room temperature magnetization but higher low-temperature magnetization than bulk YIG and its Curie temperature was in the range of 330 K to 400 K, depending on the growth conditions. First principles calculations predict that Y_{Fe} antisite defects are more stable in octahedral compared to tetrahedral Fe sites. Temperature-dependent magnetization measurements together with a superexchange dilution model and composition determined from x-ray photoelectron spectroscopy indicate that nonmagnetic species (Y^{3+} and vacancies) are predominantly accommodated in the octahedral sites but there is a significant occupancy of tetrahedral sites.

INTRODUCTION
Yttrium iron garnet (YIG, $Y_3Fe_2Fe_3O_{12}$) has been intensively studied for its useful magnetic and magnetic-optical properties since its first synthesis in the 1950s[1–3]. The garnet structure comprises three cation sites, dodecahedral (c sites), octahedral (a sites) and tetrahedral (d sites), which in YIG are occupied by Y^{3+}, Fe^{3+} and Fe^{3+} respectively. These sites may be occupied by many different cations to form stable garnets that exhibit a wide range of electronic properties. For example, Geller et al. showed that Al^{3+}, In^{3+}, Sc^{3+}, Ni^{2+}, Mn^{2+}, Si^{4+}, Ge^{4+}, Ca^{2+}, and Co^{2+} can substitute for the a site or d site Fe^{3+} in YIG, forming ferrimagnetic garnets with a range of magnetic moments, Curie temperatures and other properties[4–6]. The lattice parameter and magnetization vs. temperature of $Y_3Fe_{5-x}M_xO_{12}$ (M = In^{3+}, Sc^{3+}, Al^{3+}, Ga^{3+}) depend on the amount of substitution x and which Fe^{3+} site is occupied by the substituent[3]. Furthermore, the (c-site) Y^{3+} can be partially or completely replaced by rare earth ions such as Gd, Sm, Eu, Tb, Lu, Ho, Tm, Dy, etc. allowing the anisotropy, magnetostriction, compensation temperature and magnetization to be varied[7–9], or

by Ce^{3+} or Bi^{3+}, forming Ce:YIG or Bi:YIG with enhanced magnetooptical activity compared to that of YIG[10–14].

The site preference of cations on the a, c and d sites is primarily governed by their ionic radius, with smaller ions such as Si^{4+} or Al^{3+} preferentially occupying the tetrahedral d sites, and larger ions such as rare earths occupying the dodecahedral c sites[7,9]. Some substituents show a full range of solid solubility, such as Al, Sm or Ga in $Y_3Al_xFe_{5-x}O_{12}$[15], $Y_{3-y}Sm_yFe_5O_{12}$[16] and $Y_3Fe_{5-x}Ga_xO_{12}$ respectively[17] where $0 \leq x \leq 5$ and $0 \leq y \leq 3$, but in other cases the extent of substitution is limited to a certain level, beyond which a secondary phase will form. For example, for octahedral In^{3+} substitution ($Y_3Fe_{2-x}In_xFe_3O_{12}$), the threshold for a detectable secondary phase[18] is $x = 0.65$, while for Ca^{2+} and Ti^{4+} co-substitution, the maximum attainable value of x in the single phase garnet[19] $Y_{3-x}Ca_xTi_xFe_{5-x}O_{12}$ is 0.74.

In garnets the ideal ratio of c site to a+d site cations is 3:5. Deviations from the ideal stoichiometry may be accomodated by the formation of secondary phases, or by the presence of antisite defects, vacancies or other point defects within the garnet lattice. In the case of Y and other rare earth (R) garnets, secondary phases include binary oxides of R or Fe, or R,Fe oxides such as the perovskite-structured orthoferrite phase $RFeO_3$. The yttria-iron oxide pseudobinary phase diagram reveals that single phase YIG in air is stable over only a small range of Y:Fe ratios[20], with excess Y leading to a two-phase coexistence of YIG plus $YFeO_3$ and excess Fe leading to coexistence of YIG plus hematite (α-Fe_2O_3) or magnetite (Fe_3O_4)[2,21,22]. Similarly, $Sm_3Fe_5O_{12}$ coexists with $SmFeO_3$ or Fe_2O_3 for excess Sm or excess Fe respectively[23], and $Eu_3Fe_5O_{12}$ with $EuFeO_3$ or Fe_2O_3 for excess Eu or excess Fe respectively[24].

These results argue against the formation of significantly Y-rich or Fe-rich YIG when R:Fe differs from 0.6. However, the off-stoichiometric garnet phase may be promoted in practice by epitaxial stabilization from a garnet-structured substrate or by non-equilibrium growth methods such as vapor phase deposition. Manuilov et al[25,26] analyzed epitaxial YIG with Y:Fe up to 0.74, explaining the magnetic properties by the presence of Fe vacancies, which preferentially occupy the a sites. As another example, epitaxial TbIG films were grown by pulsed laser deposition with Tb:Fe = 0.75 and the excess Tb was assumed to be accommodated in the a sites[27]. Point defects have also been found in polycrystalline YIG, including Fe vacancies in YIG[28–30] and BiYIG[31] films grown at high oxygen pressure and Y_{Fe} antisite defects in YIG[32]. These growth processes and epitaxial stabilization enable the formation of garnet compositions that would not be stable in bulk, offering opportunities for synthesis of materials with diverse magnetic properties.

In this work, we describe the structure and magnetic properties of epitaxial YIG thin films with a considerable excess Y (Y:Fe ~ 1:1), a composition that at equilibrium would instead form the orthoferrite phase $YFeO_3$. Our results indicate that the excess Y preferably occupies the octahedral site, though there is also a significant amount of tetrahedral Y and in some cases Fe vacancies. The

nonmagnetic Fe-site point defects dilute the magnetic exchange coupling between the octahedral and tetrahedral Fe sublattices and lower the Curie temperature and the room-temperature magnetic moment of the Y-rich YIG, but raise the low-temperature moment. We use a superexchange dilution model to explain the magnetic temperature dependence of magnetization of Y-rich YIG and compare the properties to those of YIG with other a-site substituents.

EXPERIMENTAL METHODS

Epitaxial garnet films were grown on gadolinium gallium garnet (GGG) substrates with (001) and (111) orientations by pulsed laser ablation of a $YFeO_3$ (YFO) target or a $Y_3Fe_5O_{12}$ (YIG) target. During growth, the temperature at the backside of the substrate holder was maintained at T_{sub} = 900 ℃, with the substrate itself ~ 150 ℃ cooler than T_{sub}. The laser was operated at a wavelength of 248 nm with repetition rate 5 Hz. The oxygen vacancy concentration and cation stoichiometry of PLD-grown thin films are significantly affected by the growth conditions during deposition[33]. In this experiment, samples were grown under O_2 pressures of 10 or 150 mTorr and laser power 300-400 mJ/pulse (fluence of 2.0 — 2.55 J/cm^2).

Table I summarizes six Y-rich YIG samples analyzed in this work, and Tables S1 and S2 in the Supplementary Material[34] summarize these and additional samples. High resolution X-ray diffraction (HRXRD) and asymmetric reciprocal space mapping (RSM) were performed on SmartLab and Bruker D8 diffractometers with Cu $K_{\alpha 1}$ radiation (λ = 1.5406 Å) and an incident beam Ge-(220) double-bounce monochromator. Thickness was measured by X-ray reflectometry (XRR) and surface roughness by Cypher atomic force microscopy (AFM). Magnetic hysteresis loops at temperatures of 10 K — 400 K were measured using a superconducting quantum interference device (SQUID) magnetometer and a vibrating sample magnetometer (VSM), subtracting the GGG background signals using a linear fit. X-ray magnetic circular dichroism (XMCD) at the Fe $L_{2,3}$ absorption edge was collected in total fluorescence yield (TFY) mode using the beamline 4-ID-C of the Advanced Photon Source at Argonne National Laboratory at 160 K under a magnetic field H = 5000 Oe. X-ray photoelectron spectra (XPS) were collected on a PHI Versaprobe Ⅱ for composition analysis.

Density functional theory (DFT) calculations were performed with the Vienna Ab-initio Simulation Package (VASP). The Perdew-Burke-Ernzerhof (PBE) functional was used. The core-valence configurations were Y ($4s^24p^64d^15s^2$), Fe ($3p^63d^74s^1$), and O ($2s^22p^4$). The effective U for the GGA+U method was 5.3 eV for Fe. The energy cutoff was 500 eV, and k-point grids were maintained to a Monkhorst-Pack 2 × 2 × 2 mesh. All calculations were performed in a garnet unit cell that contains 8 formula units (f.u.) of $Y_3Fe_5O_{12}$, and structural characterization was performed using VESTA [35].

Table I. Summary of Y-YIG samples.

Samples	Growth Condition			Structure				Magnetism			Composition			
	O_2	Laser	rate	Thickness (t)	$\Delta d/d^a$	β^b	α^c	Ms@300K	$T_{c,exp}$	$T_{c,fit}$	ka	kd	(Y+V) :Fe[d]	Y:Fe
	mTorr	mJ	nm/h	nm	%	°	%	emu cm^{-3}	K	K	100%	100%	MFC Fit	XPS
001_Y-YIG$_1$	10	400	48.9±0.2	81.5±0.4	2.88±0.01	90.00	2.88±0.01	79±4	344	352±5	41.17	19.77	1.23	1.04
001_Y-YIG$_2$	150	300	19.8±0.1	33.0±0.1	2.13±0.01	90.00	2.13±0.01	89±5	390	388±5	32.85	17.40	1.09	1.08
001_Y-YIG$_3$	150	350	40.5±0.2	67.5±0.3	2.57±0.01	90.00	2.57±0.01	76±4	365	362±5	38.99	19.20	1.19	1.03
111_Y-YIG$_1$	10	400	45.0±0.2	125.0±0.6	3.27±0.02	88.76	0.12±0.00	65±3	335	330±5	49.15	17.40	1.29	1.07
111_Y-YIG$_2$	150	300	20.4±0.1	34.0±0.2	2.34±0.01	89.11	0.08±0.00	106±5	398	390±5	35.44	12.53	1.04	1.05
111_Y-YIG$_3$	150	350	40.5±0.2	67.5±0.3	2.73±0.01	88.96	0.10±0.00	84±4	368	362±5	40.43	17.27	1.18	1.09

[a]Out of plane lattice spacing compared to that of YIG (lattice parameter 1.237 nm).

[b]Angle between unit cell base vectors.

[c]Volume expansion ratio compared to bulk YIG.

[d]The MFC model cannot distinguish between vacancies (V) and antisite Y on the Fe sites.

RESULTS AND DISCUSSION

Structure and Composition Analysis.

HRXRD 2θ-ω scans were used to determine the structure and phase of the as-grown films on (001) and (111) orientated GGG substrates. Full range scans ($2\theta = 15—80°$) showed only garnet peaks from the substrate and film, FIG. 1 **c** with no orthoferrite peaks. Scans around the primary substrate peaks (FIG. 1 **a** and **b**) reveal that, compared with YIG films, the Y-YIG samples have a larger out-of-plane lattice spacing, greater than that of YIG by 2.5% and 2.7% for the 67 nm thick (001) and (111) samples respectively. The lattice spacing was higher for the thicker films which were formed at a higher growth rate.

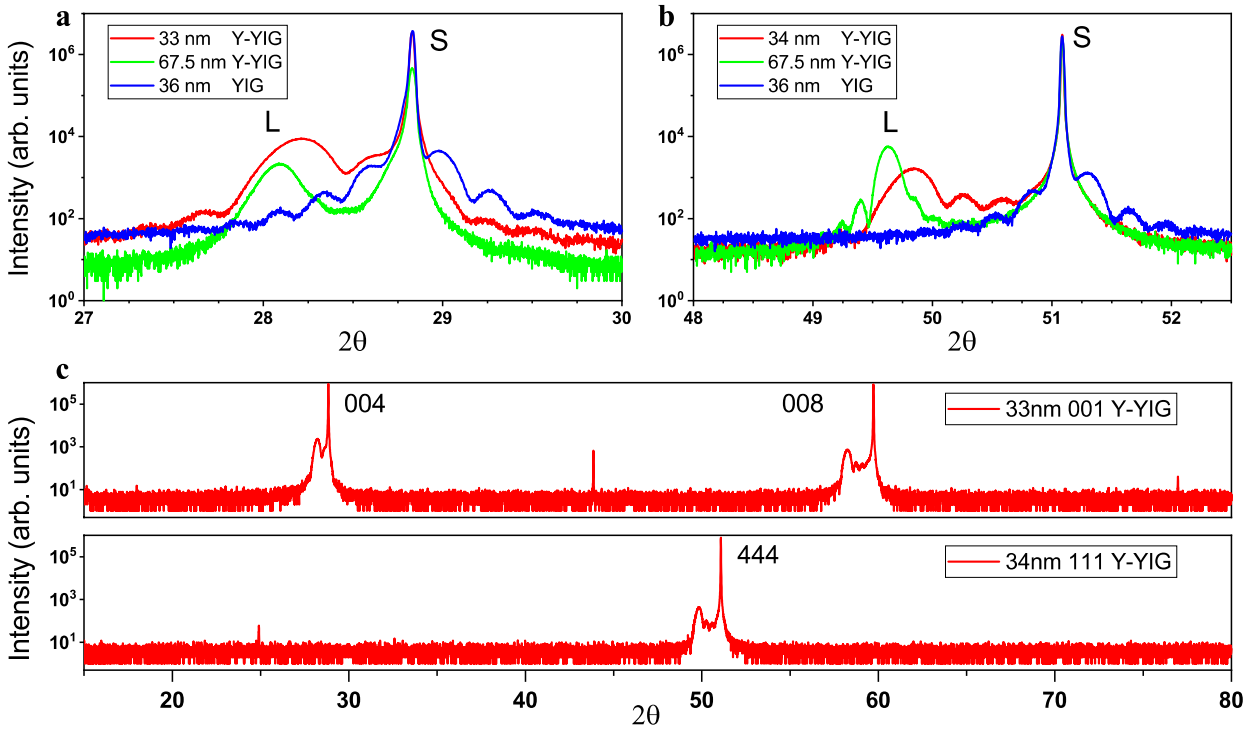

FIG. 1. X-Ray diffraction characterization. HRXRD 2θ-ω scans of (001) (a) and (111) (b) Y-YIG samples grown on GGG substrates. S represents the substrate peak, which overlaps the YIG peak, and L represents the peak from the Y-YIG films. (c) 2θ = 15—80° scan of Y-YIG$_2$ samples with (001) (top) and (111) (bottom) orientations.

The in-plane structural information of Y-YIG films was extracted from the reciprocal space maps of asymmetric diffraction peaks. For the (001) Y-YIG samples, RSMs of the (408) and (116) peaks were measured to probe the two noncollinear in-plane directions [100] and [110] respectively, whereas for the (111) samples, (642) and (664) peaks were measured to probe $[10\bar{1}]$ and $[11\bar{2}]$. Examples are shown in FIG. 2 for 33-34 nm thick Y-YIG. The RSM shows that films with thickness t < 150 nm are fully strained to match the in-plane lattice parameter of the GGG substrate.

These data show that the Y-YIG forms an epitaxial film with a coherent interface on both substrate orientations, without secondary phases. The unit cell of Y-YIG/GGG (001) is tetragonally distorted with c/a = 1.021 – 1.029, whereas the unit cell of Y-YIG/GGG (111) has a rhombohedral distortion along the body diagonal direction with corner angle of 88.8 — 89.1°. The unit cell dimensions are summarized in Table I. The (001) Y-YIG samples undergo a lattice expansion compared to bulk YIG, but the (111) Y-YIG samples have almost the same unit cell volume as bulk YIG. AFM and XRR characterization (Supplementary Material[34]) shows that the (111) Y-YIG samples have smaller surface roughness than (001) samples.

The Y:Fe ratio was quantified from the XPS spectra of Y 3d and Fe 3p peaks and normalized by the relative scattering factor. The accuracy of quantification of Y:Fe ratio is around 10 % [36] and

the results of all samples are summarized in the last column of Table I. All films had Y:Fe of 1.04 – 1.09, i.e., slightly richer in Y than the target composition, and significantly greater than the ratio of 0.6 for stoichiometric YIG.

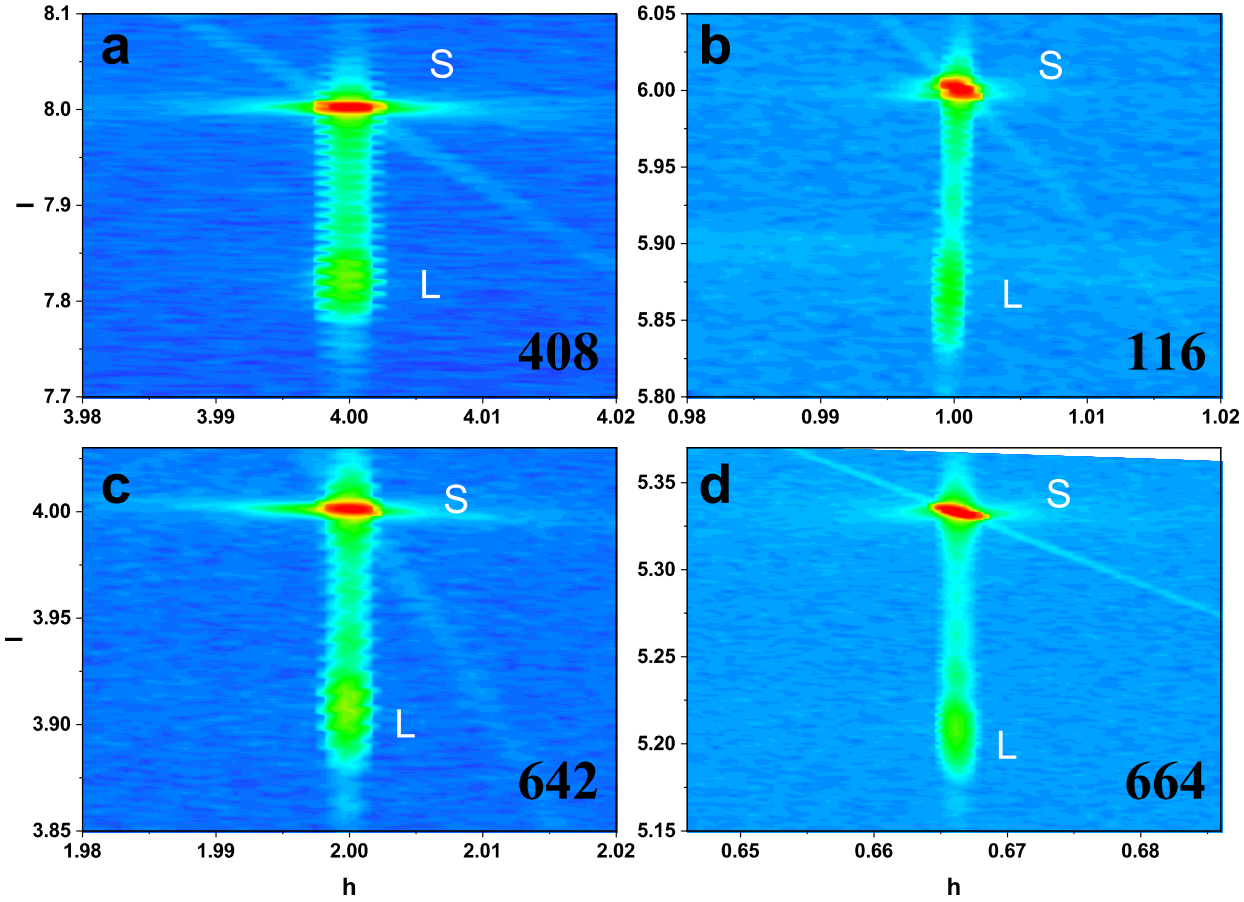

FIG. 2. RSM of Y-YIG samples. (a,b) (408) and (116) asymmetric diffraction peaks of 33 nm Y-YIG (001) sample. (c,d) (642) and (664) asymmetric diffraction peaks of 34 nm Y-YIG (111) sample. Here $h = q_x d_{mno}$ and $l = q_y d_{pqr}$ are dimensionless reciprocal vectors normalized by the substrate reciprocal lattice parameter, where q_x, q_y are reciprocal vectors of the films and d_{mno}, d_{pqr} are corresponding plane spacings of the substrate (GGG, a = 12.377 Å) . (e.g. the (408) peak is normalized to d_{001} for h and l; (642) peak to $d_{10\bar{1}}$ for h and d_{111} for l). S represents the substrate and L the film reflection.

DFT Calculations

Excess Y in the single phase garnet films may be incorporated within the structure as antisite defects where Y occupies a Fe site, or via the presence of Fe and O vacancies. Prior modeling work[20] indicates that antisite defects Y_{Fe}, Fe_Y and oxygen vacancies V_O have lower formation energies compared to cation vacancies V_{Fe}, V_Y or Frenkel defects, and Y_{Fe} is therefore likely to be the dominant defect in the Y-YIG. We modeled the magnetic and structural effects of Y_{Fe} by replacing one Fe with one Y in the YIG unit cell (8 formula units,FIG. 3 **a**) yielding Y/Fe = 0.641. The results show that the unit cell volume expanded for Y-rich YIG by 0.72% and 0.74% for

octahedral ($Y_{Fe,a}$) and tetrahedral ($Y_{Fe,d}$) antisite defects respectively. Compared to stoichiometric YIG (FIG. 3 **b**), Y antisite defects induce structural distortion (FIG. 3 **c** and FIG. 3 **d**). The Y-O bond length of the dodecahedral site decreases near the defect in common for both $Y_{Fe,a}$ and $Y_{Fe,d}$. For $Y_{Fe,a}$, the Fe-O bond length of the O shared with the d site is extended, whereas for $Y_{Fe,d}$, the Fe-O bond length for the O shared with the a site is contracted. $Y_{Fe,a}$ is more stable than $Y_{Fe,d}$ by 133 meV/f.u. indicating a site preference for Y to occupy the larger octahedral sites, which may be expected from the greater ionic radius of Y^{3+} (110 pm) compared to Fe^{3+} (65 pm). This differs from prior work[20] which predicted a lower formation energy for $Y_{Fe,d}$ compared to the $Y_{Fe,a}$.

In stoichiometric YIG, the strongest superexchange coupling is antiferromagnetic between the d site and a site Fe^{3+}. With three d-site and two a-site Fe^{3+} per formula unit, the material is ferrimagnetic with a net moment corresponding to one Fe^{3+}, i.e., 5 μ_B/f.u. at low temperatures. Because Y^{3+} has almost zero moment, the antisite Y_{Fe} is equivalent to removing an Fe^{3+} moment, which increases (decreases) the magnetization by 5 μ_B/f.u. when it is located in the octahedral (tetrahedral) site. The effect of antisite defects on the magnetism is in agreement with Ref[20].

The replacement of Fe^{3+} with Y^{3+} leads to small changes of the Y and O moments as well. In particular, Y^{3+} in a or d sites has slighly larger moments than Y^{3+} in c sites, and the small moment of $Y_{Fe,a}$ ($Y_{Fe,d}$) is parallel to that of d site (a site) Fe^{3+}. Average moments of O increase (decrease) with $Y_{Fe,a}$ ($Y_{Fe,d}$). However, these changes in the Y and O moments are minor and the main contribution to the magnetization is from the removal of Fe^{3+}.

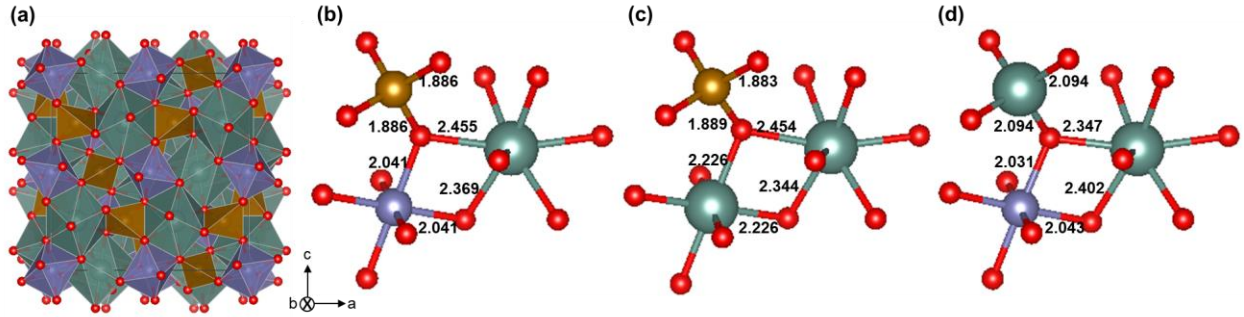

FIG. 3 (a) Unit cell of stoichiometric YIG. Green, gold, and purple corresponds to dodecahedral, tetrahedral, and octahedral sites respectively. Enlarged structure of YIG with (b) no defects, (c) a $Y_{Fe,a}$ antisite defect, and (d) a $Y_{Fe,d}$ antisite defect. Insets are bond lengths in Å.

Magnetic Properties of Y-YIG.

In plane magnetic hysteresis measurements of Y-YIG samples at different temperatures and fields up to 500 Oe are given in FIG. 4 and FIG. 5. The contribution from the paramagnetic GGG substrate is assumed to be linear for H_{max} < 500 Oe based on measurements of bare substrates and was subtracted by fitting the slope of the data at fields above 200 Oe. The remaining magnetization signal normalized by the volume of the Y-YIG is summarized in FIG. 4 **a** for a 67.5 nm thick (111)-oriented sample and FIG. 5 **a** for a (001)-oriented sample which were grown simultaneously.

At room temperature (T = 300 K), the saturation magnetization is M_{s_111} = 84 emu cm^{-3} and M_{s_001} = 76 emu cm^{-3}, which are smaller than that of bulk YIG, 140 emu cm^{-3}, or a YIG film of similar thickness (Ms_{YIG} = 137 emu cm^{-3}, t = 79 nm)[37].

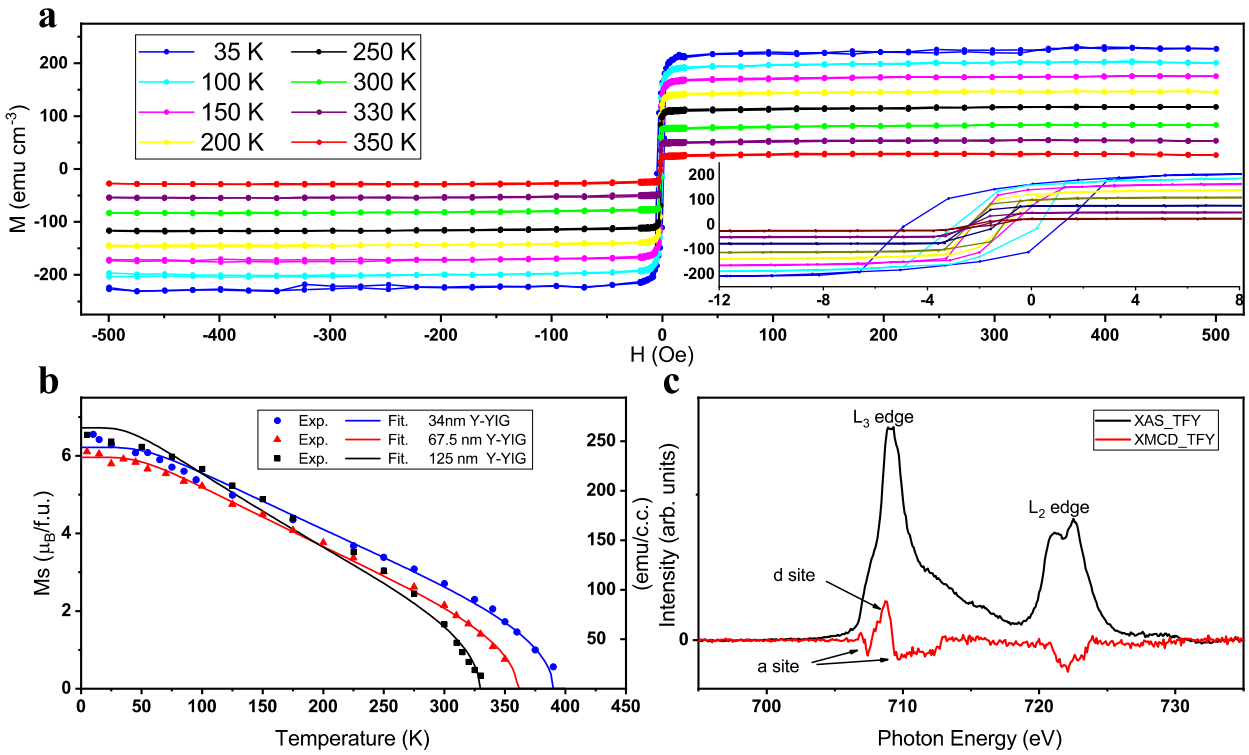

FIG. 4. Magnetic properties and XMCD measurements of (111) Y-YIG samples. (a) In-plane hysteresis loops at different temperatures of the 67.5 nm (111) Y-YIG sample. (b) Temperature dependence of saturation magnetization and fitting by Dionne's model for these three samples. (c) XMCD spectra of the 34 nm (111) Y-YIG sample.

For the (111) Y-YIG sample the saturation magnetization increases monotonically with decreasing temperature, reaching 240 ± 12 emu cm^{-3} or 6.5 ± 0.3 μ_B/f.u.. The coercivity H_c increases at lower temperatures but remains small (H_c < 4 Oe). The 3 Oe offset is attributed to the superconducting magnets[38] and not to an exchange bias. Beaulieu et al.[39] also found a monotonic increase in magnetization with decreasing temperature for (111) YIG films. However, for the (001) oriented Y-YIG samples, the coercivity is much greater, exceeding 100 Oe at 15 K, and the loops become sheared below 70 K, indicative of a change in the reversal mechanism. The saturation magnetization increases with decreasing temperature but below 70 K the saturation magnetization extracted from the 500 Oe loops starts to decrease. Mitra et al.[40] found a decrease in magnetization of (111) YIG films at low temperatures, attributed to antiparallel coupling of a ~ 6 nm thick Gd-rich garnet layer formed by interdiffusion, and Suturin et al.[41] showed a ~ 10 nm Ga-rich low-moment interdiffused layer in YIG/GGG grown by laser molecular beam epitaxy. However, we believe that the drop in magnetization in our samples has a different origin. The processing conditions used in our study are similar to those used to make TmIG/GGG films in Ref[42], which

had an interdiffused layer of only 1 nm thickness. The drop in magnetization occurred only for (001) oriented Y-YIG films and not for (111) oriented films, and the decrease was greatest for the thickest film, 001_Y-YIG$_1$, which is inconsistent with an interfacial origin. The drop in magnetization is also larger than that expected from a magnon anomaly proposed by Shimato et al.[43].

We instead attribute the decrease in magnetization of (001)-oriented samples at low temperature to incomplete saturation of the magnetization at the maximum field of the measurement. The field range was limited to 500 Oe to ensure a linear contribution from the substrate: at larger fields (H > 1000 Oe) and low temperatures (< 25 K), the GGG signal becomes large and nonlinear which precludes an accurate background subtraction. However, 500 Oe field range is inadequate to saturate the harder (001)-oriented samples at low temperatures (Supplementary Materials[34]) and the magnetization is underestimated as a result. For YIG and presumably Y-YIG the easy axis is <111> which does not lie in the film plane for either sample orientation. The film is also subject to uniaxial shape anisotropy, a growth-induced anisotropy, and magnetoelastic anisotropy terms. The higher in-plane saturation fields for (001) Y-YIG compared to (111) Y-YIG suggests higher magnetic anisotropy or greater pinning of the domain walls during reversal for this orientation.

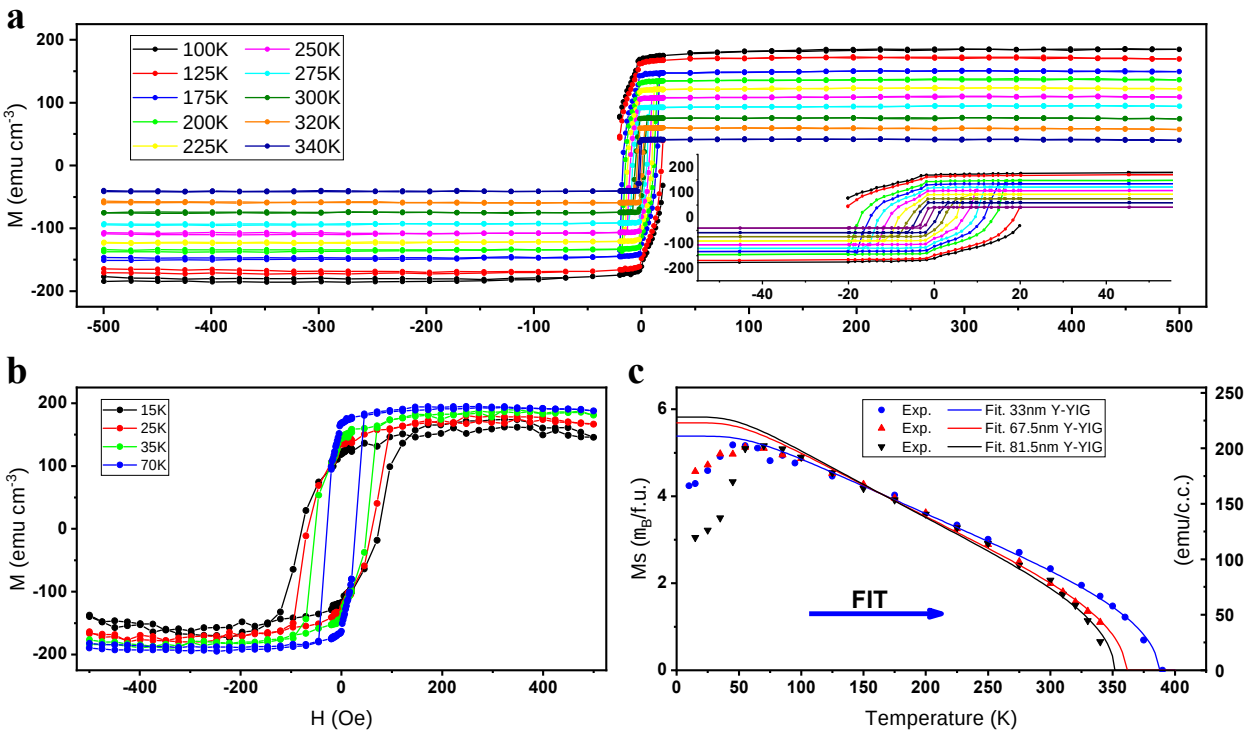

FIG. 5. Magnetic Properties of (001) Y-YIG samples. In-plane hysteresis loops obtained after subtracting linear background signal (a): T: 100 K—340 K (b): T: 15 K—70 K for the 67.5 nm thick film. (c) Magnetization measured at 500 Oe, and fitting results using Dionne's model for three samples.

Antiparallel ordering of the Fe sublattices is confirmed by XMCD measurement of a Y-YIG film, summarized in FIG. 4 **c**. The appearance of two peaks with opposite sign around the shoulders of the main peak at the L_3 absorption edge confirms that the Fe ions occupy two antiparallel sublattices, as found in YIG[44,45]. Therefore, we re-write the chemical formula of Y-YIG as $\{Y\}_3[Fe_{2\cdot(1-ka)}(Y,V_a)_{2\cdot ka}](Fe_{3\cdot(1-kd)}(Y,V_d)_{3\cdot kd})O_{12}$, where k_a and k_d stand for the fractional substitution by nonmagnetic species Y_{Fe} or vacancies V in the a and d sublattices, with $0 \leq k_a, k_d \leq 1$. From the higher formation energy of tetrahedral Y_{Fe} vs. octahedral Y_{Fe} antisite defects, we expect $k_d \ll k_a$. A preferential a-site Y occupancy is expected to lower the magnetic moment of the octahedral sublattice and increase the low temperature magnetic moment of Y-YIG compared to that of YIG[3] (~ 5 μB/f.u.). This is consistent with the extrapolated zero temperature results in Fig. 4 **b** and Fig. 5 **c**.

In order to quantitively analyze the a-site and d-site substitution, Dionne's super-exchange dilution model [46] combined with Neel's molecular field theory is used to fit the temperature dependence of saturation magnetization (FIG. 4 **b**). The expression for the molecular field coefficients of Y-YIG are adopted from Dionne's work[46] and converted to SI units:

$$N_{dd} = -345.3(1 - 0.87k_a)$$
$$N_{aa} = -738.3(1 - 1.26k_d)$$
$$N_{ad} = N_{da} = +1101.7(1 - 0.25k_a - 0.38k_d) \quad (1)$$

where k_a and k_d are the fractional substitutions defined above, and N_{ij} represents the molecular field coefficients between sites i and j.

The magnetization of each sublattice is given by:

$$M_d(T) = n_d g_d \mu_B J B_J\left(\frac{\mu_0 m}{k_B T}(N_{dd}M_d + N_{ad}M_a)\right)$$
$$M_a(T) = n_a g_a \mu_B J B_J\left(\frac{\mu_0 m}{k_B T}(N_{da}M_d + N_{aa}M_a)\right)$$
$$M(T) = |M_d - M_a| \quad (2)$$

where n_i is the volume density of Fe^{3+} of the a, d sublattices, $g_a = g_d = 2$ is the Landé factor and B_J is the Brillouin function ($J = L + S = 0 + \frac{5}{2} = \frac{5}{2}$).

Using a non-linear least square fitting algorithm from MATLAB, k_a and k_d values were obtained by fitting Dionne's model to the experimental data and the results are summarized in Table I. FIG. 4 **b** shows the fitting of (111) oriented Y-YIG samples grown at different conditions. For the (001) oriented samples the fit is carried out for the temperature range of 100 K – 400 K and the results are shown in FIG. 5 **c**.

The (Y+V):Fe ratio of Y-YIG samples can be calculated by substituting the fitted k_a and k_d values into the chemical formula $\{Y\}_3[Fe_{2\cdot(1-ka)}(Y,V_a)_{2\cdot ka}]$ $(Fe_{3\cdot(1-kd)}(Y,V_d)_{3\cdot kd})O_{12}$, and is shown in Table

I. The vacancies and Y antisite defects cannot be distinguished by the model. In the case of no vacancies, Y:Fe = $(3 + 2k_a + 3k_d)/(5 - 2k_a - 3k_d)$. For the samples Y-YIG$_2$ grown at 300 mJ laser energy and 150 mTorr oxygen corresponding to a low growth rate, the (Y+V):Fe atomic ratios calculated from the fit, 1.04 for (111)-oriented and 1.09 for (100)-oriented films agree very well with Y:Fe determined from XPS, 1.05 and 1.08 respectively, and are similar to the target stoichiometry of 1.00. This suggests that there is a negligible population of V_a and V_d and the excess Y is accommodated in the Fe sites.

For the Y-YIG$_1$ and Y-YIG$_3$ grown samples grown with lower O_2 or higher laser power corresponding to a higher growth rate, the Y:Fe ratio from XPS remains at 1.03-1.09, whereas (Y+V):Fe has a value of ~ 1.2 – 1.3. This indicates a more complex site occupancy. Table S3 in the Supplementary Material[34] shows the vacancy concentration estimated from the data, which ranges from 0.32 – 0.77 out of the 5 total a- and d-sites, though the individual occupancy of Y and V_{Fe} on each site cannot be separately determined. V_{Fe} implies the additional presence of oxygen vacancies or higher valence Fe for charge balance. These defects may also modify the parameters in the superexchange model, for example weakening the ferrimagnetic coupling and lowering the Curie temperature beyond the effects of the nonmagnetic substituents. We speculate that the greater amount of V_{Fe} proposed to exist in samples Y-YIG$_1$ and Y-YIG$_3$ is due to their faster growth rate, though a more systematic study of deposition conditions would be required to verify this.

Accomodation of Y only on the octahedral sites would imply k_a = 0.55 and k_d= 0 for a net composition of Y:Fe = 1.05. Considering the Y-YIG$_2$ samples, the fit gave k_a= 0.35 and 0.33 and k_d = 0.13 and 0.17 for the (111) and (100)-oriented samples, respectively. This indicates that the $Y_{Fe,a}$ antisite dominates, but there is also a large fraction of tetrahedral $Y_{Fe,d}$ antisite defects. The other samples also showed large amounts of $Y_{Fe,d}$. The large fraction of $Y_{Fe,d}$ may be surprising given the small size of the tetrahedral site, but the structure can distort and DFT showed that the $Y_{Fe,d}$ antisites are only modestly unfavorable compared to the $Y_{Fe,a}$ antisites. Based on the energy difference of 0.113 eV, at equilibrium at the growth temperature we would expect ~25% of the Y_{Fe} to be in tetrahedral sites. A consequence of the presence of $Y_{Fe,d}$ as well as $Y_{Fe,a}$ is the value of the low temperature saturation magnetization, which extrapolates to 6 - 6.5 μ_B/f.u. for the (111) and 5.5 μ_B/f.u. for the (001)-oriented Y-YIG films. This is larger than that of YIG (5 μ_B/f.u.) but smaller than the value expected for complete octahedral substitution of the excess Y, ~10 μ_B/f.u..

The Curie temperature of the Y-YIG samples was determined by empirical interpolation for T > 150 K based on Bloch's law: $M = M_0\left(1 - \left({}^{T}/_{T_c}\right)^{\gamma}\right)^{\delta}$ yielding a value of $T_{c,exp}$, and also from Dionne's superexchange model yielding a value $T_{c,fit}$ at M=0. The results are summarized in Table I, and show that the two methods agree to within 8 K. (Table S1 shows the Bloch law fit for the additional samples). Compared with YIG[47] (T_c = 559 K), the Curie temperature of Y-YIG is

considerably lower by 170 — 200 K. The Y substitution on both a and d sites lowers the density of Fe-O-Fe bonds and therefore weakens the intra- (within a and d) and inter- (between a and d) sublattice exchange coupling, causing a drop in Curie temperature. The Curie temperature of bulk $Y_3[In_{0.5}Fe_{1.5}](Fe_3)O_{12}$ and $Y_3[Sc_{0.75}Fe_{1.25}](Fe_3)O_{12}$ reported by Geller[3] is around 480 K and 420 K respectively, and the greater substitution for $Y_3[YFe](Fe_3)O_{12}$ implies that the Curie temperature should be even lower, which agrees with our observations. The Curie temperature of Y-YIG samples is lowest for the higher growth rate samples which is consistent with the possible presence of larger amounts of other defects such as vacancies.

The structural and magnetic results show that epitaxially-grown garnet can accommodate a large non-ideality in the Y:Fe ratio that would drive formation of other phases (i.e., the perovskite $YFeO_3$) in a bulk material or one not stabilized by epitaxy. Despite the size difference between Y^{3+} and Fe^{3+}, the data support the incorporation of excess Y by the formation of Y_{Fe} antisite defects. This occurs for both a and d sites though with a greater fraction of a-site Y_{Fe}, leading to increased low-temperature saturation magnetization compared to that of YIG. The presence of Y_{Fe} and potentially other defects, especially in high growth rate films, lowers the Curie temperature to 340 – 390 K, and the room temperature magnetization of Y-YIG is smaller than that of YIG. Excess Y therefore behaves like other non-magnetic substituents with an octahedral site preference. The formation of the Y-YIG non-equilibrium phase using pulsed laser deposition with epitaxial stabilization leads to properties that are not found in bulk garnets, and this strategy may also be extended to other thin film garnet compositions.

SUMMARY

Y-substituted YIG with a Y:Fe ratio ~ 1:1 was epitaxially grown on GGG substrates using pulsed laser deposition. There was no evidence of secondary phases, and X-ray diffraction reveals that the films have high structural quality but that the unit cell undergoes tetragonal and rhombohedral distortion for (001) and (111) oriented substrates respectively. Compared with stoichiometric YIG, the Curie temperature of Y-YIG is much lower, Tc = 330-390 K, and is sensitive to the growth conditions, and the low-temperature saturation magnetization of the Y-YIG is higher than that of YIG. The structural and magnetic data indicates that the excess Y is accomodated as antisite defects on the Fe sites. The fitting of the temperature-dependent magnetization by a superexchange model indicates that Y_{Fe} preferentially occupies the octahedral site as expected from its lower formation energy, but there is a significant amount of tetrahedral Y_{Fe} and in some cases V_{Fe} are also likely to be present. The excess Y modifies the magnetic properties of YIG in a manner that resembles that of other nonmagnetic substituents with a preference for the a sites. The key difference is that for a Y:Fe ratio ~ 1:1 the perovskite $YFeO_3$ is the thermodynamically stable phase rather than the garnet $Y_3[YFe](Fe_3)O_{12}$, and Y-YIG is only formed due to its epitaxial stabilization on a garnet substrate. We may similarly expect that other rare earth garnets $R_{3+x}Fe_{5-}$

$_xO_{12}$ could be grown with a large excess of rare earth, opening a range of interesting properties not found in bulk garnets.

Acknowledgements

The authors are grateful to Dr. Richard Rosenberg, Jackson Bauer, and Ethan Rosenberg for their help on XAS and XMCD measurements. The authors gratefully acknowledge support from NSF awards DMR 1911792 and DMR 1419807, SMART, an nCORE Center of SRC, and DARPA, and the use of MRSEC shared facilities under DMR 1419807. EC acknowledges support from a Kwanjeong Fellowship. This work also used resources of the Advanced Photon Source, a U.S. Department of Energy (DOE) office of Science User Facility operated for the DOE Office of Science by Argonne National Laboratory under contact No. DE-AC02-06CH11357.

References

1. Geller, S. & Gilleo, M. A. Structure and ferrimagnetism of yttrium and rare-earth-iron garnets. *Acta Crystallogr.* **10**, 239 (1957).
2. Nielsen, J. W. & Dearborn, E. F. The growth of single crystals of magnetic garnets. *J. Phys. Chem. Solids* **5**, 202–207 (1958).
3. Gilleo, M. A. & Geller, S. Magnetic and Crystallographic Properties of Substituted Yttrium-Iron Garnet, $3Y_2O_3{\bullet}xM_2O_3{\bullet}(5\text{-}x)Fe_2O_3$. *Phys. Rev.* **110**, 73–78 (1958).
4. Gilleo, M. A. & Geller, S. Substitution for iron in ferrimagnetic yttrium-iron garnet. *J. Appl. Phys.* **29**, 380–381 (1958).
5. Geller, S., Williams, H. J., Sherwood, R. C. & Espinosa, G. P. Substitutions of Divalent Transition Metal Ions in Yttrium Iron Garnet. *J. Appl. Phys.* **33**, 1195–1196 (1962).
6. Geller, S., Williams, H. J., Sherwood, R. C. & Espinosa, G. P. Substitutions of divalent manganese, iron and nickel in yttrium iron garnet. *J. Phys. Chem. Solids* **23**, 1525–1540 (1962).
7. Sharma, V. & Kuanr, B. K. Magnetic and crystallographic properties of rare-earth substituted yttrium-iron garnet. *J. Alloys Compd.* **748**, 591–600 (2018).
8. Lataifeh, M. S. Room temperature magnetization measurements of some substituted rare earth iron garnets. *Appl. Phys. A Mater. Sci. Process.* **92**, 681–685 (2008).
9. Sekijima, T., Kishlmoto, H., Fujii, T., Waking, K. & Okada, M. Magnetic, optical and microwave properties of rare-earth-substituted fibrous yttrium iron garnet single crystals grown by floating zone method. *Japanese J. Appl. Physics, Part 1 Regul. Pap. Short Notes Rev. Pap.* **38**, 5874–5878 (1999).
10. Uchida, H., Masuda, Y., Fujikawa, R., Baryshev, A. V. & Inoue, M. Large enhancement of Faraday rotation by localized surface plasmon resonance in Au nanoparticles embedded in Bi:YIG film. *J. Magn. Magn. Mater.* **321**, 843–845 (2009).
11. Berzhansky, V. *et al.* Magneto-optics of nanoscale Bi:YIG films. *Appl. Opt.* **52**, 6599–6606 (2013).
12. Shaposhnikov, A. N. *et al.* Modification of Bi:YIG film properties by substrate surface ion pre-treatment. *Mater. Res. Bull.* **55**, 19–25 (2014).
13. Fakhrul, T. *et al.* Magneto-Optical Bi:YIG Films with High Figure of Merit for Nonreciprocal Photonics. *Adv. Opt. Mater.* **7**, 1–9 (2019).
14. Block, A. D., Dulal, P., Stadler, B. J. H. & Seaton, N. C. A. Growth Parameters of Fully Crystallized YIG, Bi:YIG, and Ce:YIG Films With High Faraday Rotations. *IEEE Photonics J.* **6**, 1–8 (2014).
15. Yoder, H. S. & Keith, M. L. Complete substitution of aluminum for silicon: The system $3MnO \cdot Al_2O_3 \cdot 3SiO_2$—$3Y_2O_3 \cdot 5Al_2O_3$. *Am. Mineral.* **36**, 519–533 (1951).
16. Cunningham, J. R. & Anderson, E. E. Samarium Substitutions in Yttrium Iron Garnet. *J. Appl. Phys.* **31**, S45–S46 (1960).
17. Nakatsuka, A., Yoshiasa, A. & Takeno, S. Site preference of cations and structural variation in $Y_3Fe_5{-}xGa_xO_{12}$ ($0 \leq x \leq 5$) solid solutions with garnet structure. *Acta Crystallogr. Sect. B* **51**, 737–745 (1995).
18. Cunningham, J. R. & Anderson, E. E. Effect of Indium Substitution in Yttrium Iron Garnet. High Permeability Garnets. *J. Appl. Phys.* **32**, S388–S389 (1961).
19. Espinosa, G. P. A Crystal Chemical Study of Titanium(IV) and Chromium(III) Substituted Yttrium Iron and Gallium Garnets. *Inorg. Chem.* **3**, 848–850 (1964).
20. Tan, S., Zhang, W., Yang, L., Chen, J. & Wang, Z. Intrinsic defects in yttrium iron garnet:

A first-principles study. *J. Appl. Phys.* **128**, 183904 (2020).
21. Cassedanne, J. & Hebd, C. Iron-Oxygen-Yttrium Ternary Alloy Phase Diagram. *Seances Acad. Sci.* **252**, 3261–3262 (1961).
22. VAN HOOK, H. J. Phase Relations in the System Fe_2O_3–Fe_3O_4–$YFeO_3$ in Air. *J. Am. Ceram. Soc.* **44**, 208–214 (1961).
23. Galayda, A. P., Volkova, N. E., Gavrilova, L. Y., Balymov, K. G. & Cherepanov, V. A. Phase equilibria, structure and properties of intermediate phases in the Sm_2O_3 – Fe_2O_3 – CoO and Sm_2O_3 – CaO – CoO systems. *J. Alloys Compd.* **718**, 288–297 (2017).
24. Tretyakov, Y. D., Sorokin, V. V., Kaul, A. R. & Erastova, A. P. Phase equilibria and thermodynamics of coexisting phases in rare-earth element-iron-oxygen systems. I. The cerium-iron-oxygen system. *J. Solid State Chem.* **18**, 253–261 (1976).
25. Manuilov, S. A., Khartsev, S. I. & Grishin, A. M. Pulsed laser deposited $Y_3Fe_5O_{12}$ films: Nature of magnetic anisotropy i. *J. Appl. Phys.* **106**, (2009).
26. Manuilov, S. A. & Grishin, A. M. Pulsed laser deposited $Y_3Fe_5O_{12}$ films: Nature of magnetic anisotropy II. *J. Appl. Phys.* **108**, (2010).
27. Lahoubi, M. Symmetry analysis of the magnetic structures in TbIG and Tb:YIG at low temperature. *J. Phys. Conf. Ser.* **340**, 12068 (2012).
28. Dumont, Y. *et al.* Superexchange and iron valence control by off-stoichiometry in yttrium iron garnet thin films grown by pulsed laser deposition. *J. Appl. Phys.* **97**, 10G108 (2005).
29. Noun, W. *et al.* Determination of yttrium iron garnet superexchange parameters as a function of oxygen and cation stoichiometry. *Phys. Rev. B* **81**, 54411 (2010).
30. Dumont, Y. *et al.* Tuning magnetic properties with off-stoichiometry in oxide thin films: An experiment with yttrium iron garnet as a model system. *Phys. Rev. B* **76**, 104413 (2007).
31. Vertruyen, B. *et al.* Curie temperature, exchange integrals, and magneto-optical properties in off-stoichiometric bismuth iron garnet epitaxial films. *Phys. Rev. B - Condens. Matter Mater. Phys.* **78**, 1–9 (2008).
32. Chlan, V. *et al.* Antisite defects in lutetium and yttrium iron garnets prepared by liquid mix technique. *J. Magn. Magn. Mater.* **290-291 PA**, 993–996 (2005).
33. MacManus-Driscoll, J. L. *et al.* New approaches for achieving more perfect transition metal oxide thin films. *APL Mater.* **8**, 40904 (2020).
34. See Supplemental Material at [URL] for additional information on growth condition, structure, XRR, AFM and XPS quantification of Y-YIG samples; DFT calculation, Dionne's superexchange dilution model MATLAB code and data fitting; vacancy calculation and low temperature magnetometry of Y-YIG.
35. Momma, K. & Izumi, F. VESTA 3 for three-dimensional visualization of crystal, volumetric and morphology data. *J. Appl. Crystallogr.* **44**, 1272–1276 (2011).
36. Tougaard, S. Accuracy of the non-destructive surface nanostructure quantification technique based on analysis of the XPS or AES peak shape. *Surf. Interface Anal.* **26**, 249–269 (1998).
37. Onbasli, M. C. *et al.* Pulsed laser deposition of epitaxial yttrium iron garnet films with low Gilbert damping and bulk-like magnetization. *APL Mater.* **2**, 106102 (2014).
38. Buchner, M., Höfler, K., Henne, B., Ney, V. & Ney, A. Tutorial: Basic principles, limits of detection, and pitfalls of highly sensitive SQUID magnetometry for nanomagnetism and spintronics. *J. Appl. Phys.* **124**, 161101 (2018).
39. Beaulieu, N. *et al.* Temperature Dependence of Magnetic Properties of a Ultrathin Yttrium-Iron Garnet Film Grown by Liquid Phase Epitaxy: Effect of a Pt Overlayer. *IEEE Magn.*

Lett. **9**, 1–5 (2018).
40. Mitra, A. *et al.* Interfacial Origin of the Magnetisation Suppression of Thin Film Yttrium Iron Garnet. *Sci. Rep.* **7**, 11774 (2017).
41. Suturin, S. M. *et al.* Role of gallium diffusion in the formation of a magnetically dead layer at the $Y_3Fe_5O_{12}/Gd_3Ga_5O_{12}$ epitaxial interface. *Phys. Rev. Mater.* **2**, 104404 (2018).
42. Caretta, L. *et al.* Interfacial Dzyaloshinskii-Moriya interaction arising from rare-earth orbital magnetism in insulating magnetic oxides. *Nat. Commun.* **11**, 1090 (2020).
43. Shamoto, S. *et al.* Ultralow-energy magnon anomaly in yttrium iron garnet. *Phys. Rev. Res.* **2**, 33235 (2020).
44. Chin, Y. Y. *et al.* Local spin moments, valency, and long-range magnetic order in monocrystalline and ultrathin films of $Y_3Fe_5O_{12}$ garnet. *Phys. Rev. B* **99**, 184407 (2019).
45. Vasili, H. B. *et al.* Direct observation of multivalent states and $4f \rightarrow 3d$ charge transfer in Ce-doped yttrium iron garnet thin films. *Phys. Rev. B* **96**, 14433 (2017).
46. Dionne, G. F. Molecular field coefficients of substituted yttrium iron garnets. *J. Appl. Phys.* **41**, 4874–4881 (1970).
47. Anderson, E. E. Molecular Field Model and the Magnetization of YIG. *Phys. Rev.* **134**, A1581–A1585 (1964).